Impact ionization dynamics in small band-gap two-dimensional materials from a coherent phonon mechanism

Stephan Michael and Hans Christian Schneider
Department of Physics and Research Center OPTIMAS, TU Kaiserslautern, P. O. Box 3049, 67653 Kaiserslautern, Germany

(Received 30 August 2018; revised manuscript received 21 April 2019; published 23 July 2019)

For materials that exhibit dynamic changes in the electronic quasiparticle states after ultrafast optical excitation, it is extremely difficult to unambiguously separate quasiparticle band dynamics and carrier redistribution processes in state-of-the-art photoemission experiments. We study theoretically the interplay of band and carrier dynamics for a model system of a quasi-two-dimensional material with a small band gap and investigate the consequences for electronic distribution curves. Our model system contains photo-induced band-gap narrowing by a coherent phonon mechanism, which mimics the quenching of an insulator phase. We discuss the importance of impact ionization in the ultrafast response and investigate the interplay between carrier and band dynamics. Our model allows us to compare with recent experiments and identify signatures of carrier multiplication in typical electronic distribution curves as measured by time-resolved photoemission spectroscopy. We also investigate the influence of the shape of the bands on the carrier multiplication.

DOI: 10.1103/PhysRevB.100.035431

I. INTRODUCTION

Recent developments in time- and angle-resolved photoemission spectroscopy (trARPES) have opened up the possibility to study the material response after ultrafast optical excitation using photoemission techniques [1–3]. This progress has facilitated the study of correlated and nanoscale quantum materials [4]. Besides graphene [5–9], other two-dimensional materials [10], in particular transition-metal dichalcogenides (TMDC) [11–13], have been the center of current investigations. Associated with this topic is an active interest in metal-insulator transitions [14]. Besides Mott insulators [13,15–20] these transitions can appear as excitonic and Peierls insulators, where a formation of a charge density wave (CDW) and a periodic lattice distortion occur [21]. However, charge density waves are observed in many solids and their origin is still under debate [22–26]. Further, changing the symmetry of a material via optically induced phase transitions offers new ways to manipulate material properties on ultrafast timescales [27,28]. Research about the ultrafast response of two-dimensional materials like TMDC in connection with their rich electronic phase diagrams, e.g., superconductivity [29,30] or CDW phases, may well be important for understanding the basic physics for the design of future ultrafast (optoelectronic or optospintronic) devices [31–33]. If one is interested in, e.g., photoresponse and/or photocurrents in this new type of materials, then the effects of impact ionization as the cause of carrier multiplication become important. In this context a lot of research has been done on graphene [34–42], carbon nanotubes [43–49], and recently also on TMDCs [50–55].

Materials like 1*T*-TaS_2, 2*H*-$TaSe_2$, and 1*T*-$TiSe_2$ have been studied in some detail [56–58], but there still is a controversy about the origin of the CDW phases in those materials, especially for 1*T*-$TiSe_2$. In Refs. [59–68] an excitonic insulator mechanism was identified. However, there are also arguments that an electron-lattice interaction with the help of the Jahn-Teller effect leads to a Peierls-like CDW transition and the accompanying opening of a gap [69–72]. To our knowledge, the prevailing explanation is a combination of exciton-formation and electron-phonon coupling [65–67,70,72–82]. In this context, the chirality of the CDW [83–86] and a softening of phonon modes [81,87] have also been discussed.

On the basis of experimental results and a simple model calculation, it has recently been argued in Ref. [88] that in 1*T*-$TiSe_2$ excitation by an ultrafast optical pulse induces carrier multiplication and gap-closing dynamics, which amplify each other during the quenching of the CDW phase.

The present paper is devoted to a study of nonequilibrium carrier dynamics during an optically induced phase change between an "insulator" and a "metallic" phase in a system with a small band gap, where carrier-scattering processes may lead to carrier multiplication due to impact ionization. In particular, we investigate in more detail than we did in Ref. [88] the interplay between carrier dynamics/carrier multiplication and quasiparticle band-structure change/gap quenching. We employ a dynamical model that is capable of describing aspects of the ultrafast response of small band-gap two-dimensional (2D) materials, assuming an electron-phonon-based mechanism behind the formation of the CDW state. We do not attempt a microscopic description of the complete change between insulator and metallic phase, but restrict our attention to the onset of the phase transition starting from the CDW insulator phase, and model the relevant lattice dynamics by coherent phonons. These coherent phonons interact with the optically excited electronic dynamics and, in turn, change the quasiparticle band structure via a modulation of hybridization between electronic orbitals centered at the ions that oscillate with the coherent phonon. For this concrete mechanism, we study the interplay between carrier multiplication effects and quasiparticle band-structure dynamics, and we explore the consequences for quantities accessible in recent experiments, where carrier multiplication and band-strucure dynamics

cannot easily be disentangled [88]. In particular, we study the influence of different excitation scenarios and compare the results for different band structures (parabolic and Mexican-hat-shaped bands).

The outline of this paper is as follows. In Sec. II we first introduce a model composed of a tight-binding band structure and carrier-phonon interaction in which the quenching of the insulator phase is due to the coupling to coherent phonons. In a nonequilibrium situation, this electron-phonon coupling results in the change in quasiparticle bands associated with a Peierls-like transition. In Sec. III we set up the equations of motion for the relevant distribution functions including the optical-excitation contribution and Coulomb interaction. Numerical results are presented in Sec. IV. We discuss here in particular the influence of model parameters on the carrier dynamics, the interplay of carrier multiplication, and gap-closing dynamics and their signatures in electronic distribution curves. Technical details concerning the tight-binding model and the numerical solution of the dynamical equations including the gap dynamics are collected in Appendices A and C. We conclude the paper in Sec. V.

II. QUASIPARTICLE ELECTRONIC STRUCTURE CALCULATION

As we want to describe carrier dynamics that accompany the quenching of a small band-gap insulator phase, we first need to address how the quasiparticle band structure changes during this phase transition. While a variety of different models for charge-density-wave insulators exist [22], the classification for materials like $1T$-$TiSe_2$ or $1T$-TaS_2 is not straightforward. Among other reasons, this is because electron-electron and electron-phonon interactions may both play an important role in the phase transition dynamics. As we focus here on the carrier dynamics, it is beyond the scope of this paper to include such complex interdependencies. Instead of determining the insulator phase from the normal phase, we start from a TB model of the band structure in the insulator phase and describe the quenching of this phase as an effective misalignment of the atomic positions of the different atoms in the unit cell. This effective atomic displacement after an optical excitation enters our calculation as a coherent phonon.

A. Tight-binding model

We employ a tight-binding model to describe a quasi-two-dimensional material with two atomic species A_d and A_p in the insulator phase. The parameters are chosen such as to reproduce some important characteristics of electronic states in TMDCs. In the case of a TMDC, the atomic species A_d is the transition metal (e.g., Ti) with d-type or f-type valence orbitals and the atomic species A_p is the chalcogen (e.g., Se) with p-type valence orbitals. For instance, in Refs. [74,76] it was found that for $1T$-$TiSe_2$ only the three hopping parameters dd_σ, pp_σ, and pd_π contribute significantly to the behavior of states with energies close to the Fermi energy. This allows one to use a restricted model that includes only these hopping parameters.

As we do not attempt a microscopic model of the physics underlying the phase transition and as we are mainly interested in the electronic dynamics close to the small band gap, which is the indicator of the CDW and typically opens at high symmetry points, such as Γ or M points, we use a simple two-band tight-binding model to capture the characteristics of the carrier and band dynamics around the gap after an ultrashort optical excitation. We explain the relation of this ansatz to existing tight-binding models of transition-metal dichalcogenides in Appendix A. For now, we take the model tight-binding Hamiltonian in the form

$$\begin{aligned} H_{\mathrm{TB}} = {} & \epsilon_0^p \left(c_{\mathbf{k}}^{ps}\right)^\dagger c_{\mathbf{k}}^{ps} + \epsilon_0^c \left(c_{\mathbf{k}}^{ds}\right)^\dagger c_{\mathbf{k}}^{ds} \\ & + 2V_{pp}[\cos(k_x e_x) + \cos(k_y e_y)]\left(c_{\mathbf{k}}^{ps}\right)^\dagger c_{\mathbf{k}}^{ps} \\ & + V_{pd}\left(c_{\mathbf{k}}^{ps}\right)^\dagger c_{\mathbf{k}}^{ds} + V_{dp} c_{\mathbf{k}}^{ds\dagger} b c_{\mathbf{k}}^{ps} \\ & + 2V_{dd}[\cos(k_x e_x) + \cos(k_y e_y)]\left(c_{\mathbf{k}}^{ds}\right)^\dagger c_{\mathbf{k}}^{ds}, \end{aligned} \tag{1}$$

where ϵ_0^p, ϵ_0^d are the on-site energies; V_{pp}, V_{pd}, V_{dp}, and V_{dd} are the tight-binding coupling-elements; and $\mathbf{e}$ is the distance vector between two neighboring unit cells. As we do not include spin-orbit coupling, we do not explicitly write out the spin dependence s in the following.

This model yields a conduction band mainly consisting of a d-type transition metal orbital and a valence band mainly originating from a p-type chalcogen orbital. In the neighborhood of this point the band structure has the shape of a Mexican hat with a small band gap and pronounced band mixing for the model parameters chosen here, see Sec. IV. Close to the high symmetry point the band structure possesses rotational symmetry. We stress that the simplicity of this model and the high symmetry are not too restrictive, because a fast angular redistribution of carriers due to electron-phonon scattering [89] will smooth out the effects of anisotropy, and our results should also be transferable to nonparabolic band structures.

B. Quasiparticle band dynamics and the effective Hamiltonian

This subsection is concerned with determination of the carrier states that accompany the onset of the phase change and that we will sometimes refer to simply as "band dynamics." We do not attempt a microscopic *ab initio* description of the coupled electron-ion system and the transition from normal phase to charge-density wave phase. Instead, we use an effective Hamiltonian for the system in the charge-density wave state that already incorporates the lattice distortion induced by the electron-phonon interaction. Using the language of dynamical correlation functions for the electron-phonon interaction, the coherent phonon is the lowest order contribution, as shown, e.g., by Rossi and Kuhn [90]. In the next order one finds scattering and dephasing terms, but only the coherent phonon mode leads to a permanent ionic displacement and is therefore important for the band-structure change. The ionic displacement causes a change of the hybridization between electronic orbitals centered at different ions, which changes the effective Hamiltonian. Due to the dependence on the phonon dynamics, the effective Hamiltonian becomes time dependent.

We begin with the free phonon Hamiltonian and the electron-phonon interaction which we will then specialize to

the case of a coherent phonon. Free phonons are described by

$$H_{\mathrm{pn}} = \hbar \sum_{\mathbf{q},\lambda} \omega_{\mathbf{q},\lambda} \left(b^{\dagger}_{\mathbf{q},\lambda} b_{\mathbf{q},\lambda} + \frac{1}{2} \right), \tag{2}$$

where λ is the phonon mode. The electron-phonon coupling is

$$H_{\text{e-pn}} = \sum_{\mathbf{q},\lambda} \sum_{\mathbf{k},b_1,b_2} g^{\lambda,b_1,b_2}_{\mathbf{q},\mathbf{k}} (b_{\mathbf{q},\lambda} + b^{\dagger}_{-\mathbf{q},\lambda}) (c_{\mathbf{k}+\mathbf{q},b_1})^{\dagger} c_{\mathbf{k},b_2}, + \text{H.c.}, \tag{3}$$

where $g^{\lambda,b_1,b_2}_{\mathbf{q},\mathbf{k}}$ is the electron-phonon matrix element and b_1, b_2 the band indices.

We now specialize the above expressions for a coherent phonon (cpn) with $\mathbf{q} = \mathbf{0}$ that leads to a distortion consistent with the symmetry of the material, e.g., the A1g mode, in which the two kinds of atoms are displaced in the unit cell. The coherent phonon couples to the electrons by modulating the *p*-*d* hybridization

$$H_{\text{e-cpn}} = \sum_{\mathbf{k}} g^{pd}_{\mathbf{0}} (b_0 + b^{\dagger}_0) \left(c^{p}_{\mathbf{k}+\mathbf{0}}\right)^{\dagger} c^{d}_{\mathbf{k}} + \text{H.c.}, \tag{4}$$

where $g^{pd}_{\mathbf{0}}$ is the matrix element for the coupling of electrons to the coherent phonon in the orbital basis. We assume for simplicity that the corresponding matrix element is independent of $\mathbf{k}$. The interaction of electrons with such a coherent phonon leads to a mean-field contribution,

$$H^{(\mathrm{mf})}_{\text{e-cpn}} = \sum_{\mathbf{k}} \sum_{l_1,l_2} g^{l_1 l_2}_{0} (B_0 + B^{\dagger}_0) c^{l_1 \dagger}_{\mathbf{k}+\mathbf{0}} c^{l_2}_{\mathbf{k}} + \text{H.c.}, \tag{5}$$

where $B_0 = \langle b_0 \rangle$ is the coherent phonon amplitude and $l_1, l_2 \in \{p, d\}$ denotes the orbital index. The mean-field part of the coupling Hamiltonian to the coherent phonon does not contain phonon operators and can be combined with H_{TB} to an effective Hamiltonian for the carrier system that describes the states around the Fermi energy

$$H_{\mathrm{eff}} = H_{\mathrm{TB}} + H^{(\mathrm{mf})}_{\text{e-cpn}}. \tag{6}$$

As H_{eff} is time dependent its eigenvalues $\epsilon_{b,\mathbf{k}}$ and eigenvectors $\Psi_{b,\mathbf{k}}(\mathbf{r})$ are calculated for every time step of the dynamical calculation. Thus, matrix elements $g^{b_1 b_2}_{0}$ and $\rho^{b_1 b_2}_{\mathbf{k}}$ generally involve time-dependent basis states as will be discussed in Appendix C. In this time-dependent eigenbasis, $n^{b}_{\mathbf{k}} = \rho^{bb}_{\mathbf{k}}$ can be interpreted as the occupation of the state $|b, \mathbf{k}\rangle$ at that time and $g^{b_1 b_2}_{0,\mathbf{k}}$ the corresponding phonon matrix element. In particular, the matrix element g^{pd}_{0} in the orbital basis is related to matrix elements $g^{cc}_{0,\mathbf{k}}$ and $g^{vv}_{0,\mathbf{k}}$ in the time-dependent basis. Assuming that the coherences in this equation of motion die out faster than the dynamics of interest, we obtain the equation of motion

$$\begin{aligned} \frac{d}{dt} B_{\mathbf{0}} &= -\left(i\omega_{\mathbf{0}} + \gamma^{P}_{\mathrm{deph}}\right) B_{\mathbf{0}} + \frac{1}{i\hbar} \sum_{\mathbf{k}} \sum_{b} \left[\left(g^{bb}_{0,\mathbf{k}}\right)^{*} n^{b}_{\mathbf{k}} \right] \\ &= -\left(i\omega_{\mathbf{0}} + \gamma^{P}_{\mathrm{deph}}\right) B_{\mathbf{0}} \\ &\quad + \frac{1}{i\hbar} \left[\sum_{\mathbf{k}} \left(g^{cc}_{0,\mathbf{k}}\right)^{*} n^{c}_{\mathbf{k}} + \sum_{\mathbf{k}} \left(g^{vv}_{0,\mathbf{k}}\right)^{*} n^{v}_{\mathbf{k}} \right]. \end{aligned} \tag{7}$$

The coupling matrix elements g^{pd}_{0}, which are off diagonal with respect to the orbital index, influence the band occupations $n^{b}_{\mathbf{k}}$ via $g^{bb}_{0,\mathbf{k}}$ matrix elements, which are diagonal with respect to the band index and thus drive the coherent phonon amplitude Eq. (7).

Counterintuitive to Eq. (7), where a compensation between electron and hole contributions could be expected, we have an additive contribution due to the different sign of the electron-phonon coupling constant for the two bands after the basis transformation. This leads to an additional contribution to the gap closing by the carrier multiplication. This is explained in more detail in Appendix B.

The contribution of the fully occupied valence band in Eq. (7) is subtracted from the coherent phonon amplitude because the effective Hamiltonian for the system in the CDW state already incorporates the corresponding lattice distortion induced by the electron-phonon interaction. In our two-band model the hole distribution in the v' band is neglected in the calculation of the coherent phonon amplitude. If the optical excitation would directly couple the conduction band c and valence band v, then the effects of the band-gap narrowing would be stronger for the same strength of the phonon coupling constant. However, as we do not attempt a material realistic description and instead focus on the photo-induced band-gap narrowing by a coherent phonon mechanism in a two-band tight-binding model, the electron-phonon coupling constant is only an effective parameter to characterize the strength of the interplay between band and carrier dynamics. Effects of additional phonon modes or band contributions would unnecessarily bedevil the understanding of the model system and for the sake of simplicity are incorporated in this effective parameter.

III. CARRIER DYNAMICS VIA EQUATION OF MOTION TECHNIQUE

A. Optical excitation

We model the optical excitation after a recent experiment on 1T-$TiSe_2$ in Ref. [88], where carriers were excited with an 1.6-eV pulse around 200 meV above the Fermi level into a Ti $3d$ band around the M point. A sketch of the band structure around such a high symmetry point is contained in Fig. 1. In this region of the band structure, only a small band gap exists between the Ti $3d$ band and a back-folded Se $4p$ band. As the holes, which are likely created in a Se $4p(x, y)$ bands, never appear close to the Fermi surface, we do not include these band states in our two-band tight-binding model. Further, the dispersions of the bands of interest are different (i.e., have very different curvature in our simplified case), so that in the first few hundred femtoseconds the excited holes have no chance to reach the Fermi surface and no efficient contribution to the ultrafast carrier and band response around Fermi surface is possible, as found in experiment [88]. Thus, we model the optical excitation between the conduction band "c" mainly originating from the d-type orbital of atom species A_d and a third band v' below the Fermi surface by

$$\left.\frac{d}{dt} p^{b_1 b_2}_{\mathbf{k}}\right|_{\mathrm{opt}} = -\left(i\omega^{b_1 b_2}_{\mathbf{k}} + \gamma^{P}_{\mathrm{deph}}\right) p^{b_1 b_2}_{\mathbf{k}} - i\Omega^{b_1 b_2}_{\mathbf{k}} \left(n^{b_1}_{\mathbf{k}} - n^{b_2}_{\mathbf{k}}\right) \tag{8}$$

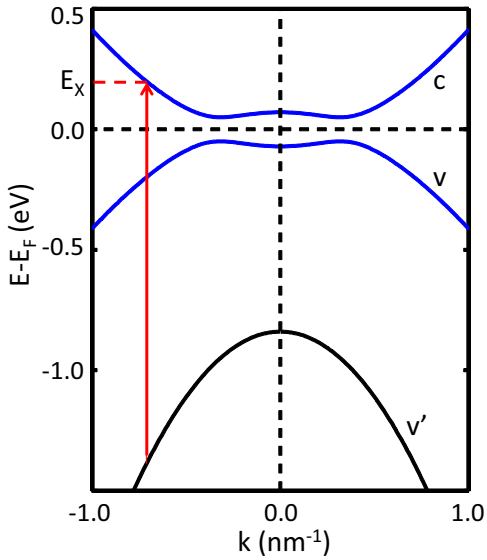

FIG. 1. Band structure of the unexcited material on a high symmetry point in the Brillouin zone on the Fermi surface in radial in-plane direction. The blue curves are the conduction band c and the valence band v calculated from the tight-binding Hamiltonian. The black curve is a third band $v\prime$ not included in the two-band tight-binding model far below the Fermi surface used for the ultrafast optical excitation with a 1.6-eV pulse (red arrow). The vertically dashed line is the Fermi surface and the horizontal dashed line is the high symmetry point in the Brillouin zone.

and

$$\left.\frac{d}{dt}n_{\mathbf{k}}^{b_1}\right|_{\text{opt}} = -\left(i\Omega_{\mathbf{k}}^{b_1b_2}p_{\mathbf{k}}^{b_1b_2} + \text{H.c.}\right), \tag{9}$$

where $b \in \{\text{c}, v'\}$, and we have again suppressed the spin index.

The major contribution to the coherent phonon amplitude dynamics originates from the excitation of electrons into the conduction band. This is in accordance to situations where optical excitation can trigger a displacive A1g CDW amplitude mode by exciting electrons from bonding to antibonding states, e.g., in $1T$-$TiSe_2$ [80]. It is also supported by other investigations, which have found that the A1g mode shows a strong coupling to conduction electrons [91,92]. While the effects of excitonic contributions likely have to be included to obtain quantitative agreement (e.g., for the speed of the gap dynamics) [88], the qualitative picture of the onset of a phase transition due to ultrafast optical excitation can be described by coherent phonons. In such a model, carrier multiplication also has an contribution to the dynamics of the coherent phonon amplitude, as we show in the following.

B. Carrier-carrier Coulomb scattering

The carrier dynamics due to Coulomb scattering in the first few hundred femtoseconds after the ultrafast optical excitation is also included in the equation of motion for the density matrix. As the Coulomb interaction leads to transitions between quasiparticle states, which change dynamically, we use time-dependent Bloch states. This entails not only the correction of the band energies but also a recalculation of the interaction-matrix elements. In general, it is associated with a transformation of diagonal density contributions $n_{\mathbf{k}}^{b}$ into off-diagonal coherence contributions in conjunction with correlated correction-terms in the equation of motion. This general consequences are described and the level of approximation for the system under investigation is explained in Appendix C, where we assume a sufficiently high dephasing for these coherences, which is likely for the system under investigation, and hence the off-diagonal coherence contributions in conjunction with correlated correction-terms in the equation of motion can be neglected. Thus, we implement the time-dependent basis in the description of the carrier dynamics using time-dependent band energies and wave functions including time-dependent Coulomb matrix elements due to the basis transformation, which also include screening that is time dependent due to the changes the density of excited carriers. Importantly, the band dynamics here leads to an additional redistribution of carriers into the new equilibrium distribution and changes the ratio between intra and interband scattering pathways.

The derivation of the Coulomb scattering equations itself can be established in various ways, for instance, with cluster expansion techniques or with the Green's function technique under the use of the Kadanoff-Baym equations by applying the second-order Born approximation for the self-energy [13]. For the carrier-carrier scattering we neglect coherences and obtain the following equation of motion for the Coulomb scattering in Markov approximation:

$$\frac{d}{dt}n_{\mathbf{k}}^{b} = \frac{2\pi}{\hbar}\sum_{\mathbf{k}_2\mathbf{k}_3}\sum_{b_2b_3b_4}\widehat{W}(N^{\text{in}} - N^{\text{out}})\delta(\Delta\epsilon) \tag{10}$$

with

$$\widehat{W} = W_{\mathbf{k}\mathbf{k}_2\mathbf{k}_3\mathbf{k}_4}^{bb_2b_3b_4}\left(W_{\mathbf{k}\mathbf{k}_2\mathbf{k}_3\mathbf{k}_4}^{bb_2b_3b_4*} - W_{\mathbf{k}\mathbf{k}_2\mathbf{k}_4\mathbf{k}_3}^{bb_2b_4b_3*}\right), \tag{11}$$

$$N^{\text{in}} = \left(1 - n_{\mathbf{k}}^{b}\right)n_{\mathbf{k}_2}^{b_2}\left(1 - n_{\mathbf{k}_3}^{b_3}\right)n_{\mathbf{k}_4}^{b_4}, \tag{12}$$

$$N^{\text{out}} = n_{\mathbf{k}}^{b}\left(1 - n_{\mathbf{k}_2}^{b_2}\right)n_{\mathbf{k}_3}^{b_3}\left(1 - n_{\mathbf{k}_4}^{b_4}\right), \tag{13}$$

$$\Delta\epsilon = \epsilon_{\mathbf{k}}^{b} - \epsilon_{\mathbf{k}_2}^{b_2} + \epsilon_{\mathbf{k}_3}^{b_3} - \epsilon_{\mathbf{k}_4}^{b_4}, \tag{14}$$

where $W_{\mathbf{k}\mathbf{k}_2\mathbf{k}_3\mathbf{k}_4}^{bb_2b_3b_4}$ are the screened Coulomb-matrix elements, $n_{\mathbf{k}}^{b}$ is the carrier distribution, and $\epsilon_{\mathbf{k}}^{b}$ the corresponding energy on $\mathbf{k}$ for the band $b \in \{\text{c}, v\}$. The spin-index s is neglected. We would like to add a remark on the validity of the Markov approximation, which is usually based on time-independent energies. The time dependence in quasiparticle bands affects the energy conserving δ function, i.e., the spectral part of Eq. (10). Even though the changes in quasiparticle bands described below are not small, the heated quasiequilibrium that results after optical excitation is more influenced by the carrier redistribution in the bands, i.e., the kinetic part of Eq. (10). We therefore keep Eq. (10) in the Markov form with the energy-conserving δ function.

The screened Coulomb potential is

$$W_{\mathbf{k}\mathbf{k}_2\mathbf{k}_3\mathbf{k}_4}^{bb_2b_3b_4} = \sum_{\mathbf{q}} w(\mathbf{q})I_{\mathbf{k}\mathbf{k}_4}^{bb_4}(\mathbf{q})I_{\mathbf{k}_2\mathbf{k}_3}^{b_2b_3}(-\mathbf{q}) \tag{15}$$

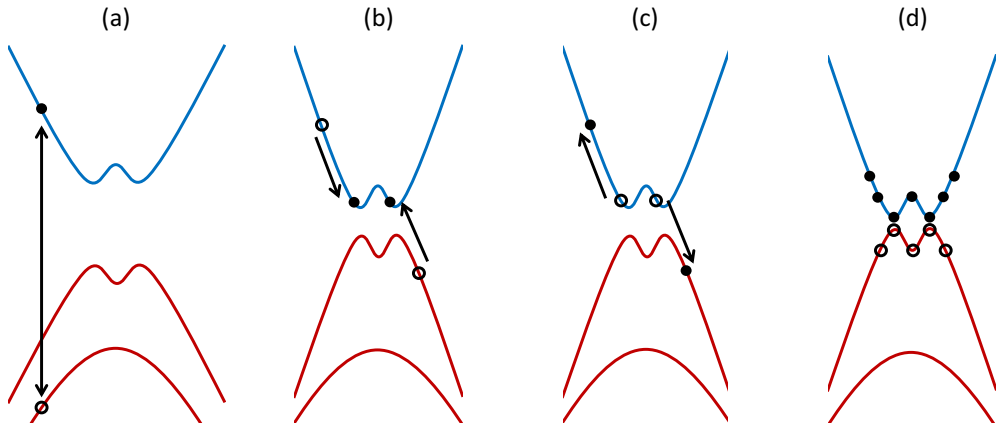

FIG. 2. Schematic picture of (a) the optical excitation, (b) impact ionization processes, (c) Auger recombination processes, and (d) the quasiequilibrium situation in the quenched CDW phase, which is reached a few hundred fs after the optical excitation. The red bands are valence bands and the blue band is the conduction band. For the transitions in (a)–(c), initial carrier states are denoted by open circles and final states by filled circles. For the quasiequilibrium situation in (d) occupied electron and hole states are indicated by open and filled circles, respectively.

with the overlap integrals

$$I^{bb_4}_{\mathbf{k}\mathbf{k}_4}(\mathbf{q}) = \int \Psi^b_{\mathbf{k}}(\mathbf{r})^* e^{i\mathbf{q}\mathbf{r}} \Psi^{b_4}_{\mathbf{k}_4}(\mathbf{r})\, d^3r \tag{16}$$

and $w(\mathbf{q}) = \varepsilon^{-1}(\mathbf{q})v(\mathbf{q})$. Further, $\Psi^b_{\mathbf{k}}(\mathbf{r})$ are the eigenfunctions of the time-dependent tight-binding Hamiltonian in Eq. (6), $v(\mathbf{q})$ is the unscreened Coulomb potential including a background dielectric constant ε_b, and A the normalization area.

In the derivation of the Coulomb scattering equations, the screened Coulomb potential can be naturally included. The screening of the Coulomb interaction is time dependent as the density of excited carriers changes. This effect is taken into account using the static limit of Lindhard dielectric function

$$\varepsilon(\mathbf{q}) = 1 - \frac{1}{A}\sum_{\mathbf{k},b} V^{bbbb}_{\mathbf{k},\mathbf{k}-\mathbf{q},\mathbf{k},\mathbf{k}-\mathbf{q}} \frac{n^{\lambda}_{\mathbf{k}-\mathbf{q}} - n^{\lambda}_{\mathbf{k}}}{\epsilon^{\lambda}_{\mathbf{k}-\mathbf{q}} - \epsilon^{\lambda}_{\mathbf{k}}}, \tag{17}$$

where $V^{bb_2b_3b}_{\mathbf{k},\mathbf{k}_2,\mathbf{k}_3,\mathbf{k}_4}$ are the Coulomb-matrix elements calculated from the unscreened Coulomb potential $v(\mathbf{q})$.

IV. NUMERICAL RESULTS

A. Overview of calculational setup

To investigate the ultrafast response of a small band-gap 2D material after an ultrafast optical excitation, and particularly of the role of impact ionization and carrier multiplication in the conduction band, we assume the setup shown in Fig. 1, which we discuss here first. From the tight-binding Hamiltonian Eq. (1) from Sec. II A, we obtain two Mexican-hat-shaped bands close to the Fermi surface, a conduction band "c" and a valence band "v." Further, we assume a lattice temperature of 100 K and the band gap is measured as the nearest distance between the two Mexican-hat-shaped bands, which is 100 meV for the unexcited band structure. The lattice temperature is below the transition temperature and the band gap is adapted to that of the CDW phase of a typical material like $TiSe_2$ as reported, for example, in Ref. [60]. The optical excitation is modeled as originating from a third band "v'" not included in the two-band tight-binding model, see Sec. III A. As indicated in Fig. 1, the v' band is far below the Fermi surface and the ultrafast optical excitation by a pulse with a 1.6-eV photon energy excites carriers into the conduction band around 200 meV above the Fermi surface as measured by trARPES experiments on $TiSe_2$ reported in Ref. [88]. For the unexcited material we assume Fermi distributions and thus obtain a nearly empty conduction band with negligible band corrections due to coherent phonons, see Sec. II B, and a weak screening.

An overview of the carrier and band dynamics that we study quantitatively in the following is given in Fig. 2. After the ultrashort optical excitation shown in Fig. 2(a), different effects are indicated in Figs. 2(b)–2(d). The band dynamics induced by coherent phonons is shown as the narrowing of the gap and a change of the band curvature. The band dynamics are coupled to carrier redistribution processes due to Coulomb scattering. Besides carrier-carrier intraband scattering processes, interband scattering processes such impact ionization as illustrated in Fig. 2(b) and the reverse process, Auger recombination, as depicted in Fig. 2(c), are included in our treatment of Coulomb scattering, see Sec. III B. A few hundred femtoseconds after the optical excitation a quasiequilibrium in a quenched CDW phase is reached, as illustrated in Fig. 2(d).

B. Characteristics of band and carrier response

First, we discuss the essential characteristics of the dynamical results for the excitation described above. A technical aspect is to clarify and investigate the effect of the basis transformation of the electron-phonon matrix element between the time-dependent basis of band states and the atomic eigenbasis, which creates k-dependent phonon matrix elements from initially constant values in the atomic eigenbasis.

The Mexican-hat-shaped electronic band structure shown in Fig. 1 is modeled using the tight-binding parameters $\epsilon^p_0 = 1.95\,\text{eV}$, $\epsilon^d_0 = -1.95\,\text{eV}$ for the on-site energies and $V_{pp} = -V_{dd} = -0.5\,\text{eV}$, $V_{pd} = 0.05\,\text{eV}$ for the coupling

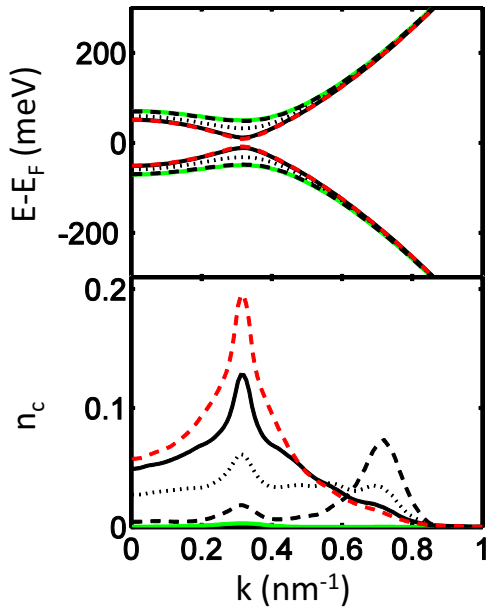

FIG. 3. Band dynamics (top) and carrier distribution in the conduction band (bottom) at −25 fs (solid green), 25 fs (dashed black), 100 fs (dotted black), 175 fs (solid black), and 250 fs (dashed red) after an ultrashort optical excitation by a $\sigma_T = 14$ fs pulse centered at 0 fs. Between -25fs and 25 fs the optical excitation mainly determines the carrier dynamics and the nonequilibrium carrier distribution lead to a closing of the gap. After 25 fs the optical excitation does not contribute any more. Now the carrier scattering and the effect of gap closing increase the impact ionization, which contributes to a further gap closing until a quasiequilibrium after about 200 fs is reached.

elements. For the coherent phonons, we take $\hbar\omega_0 = 12.4$ meV and $\gamma^P_{\text{deph}} = 5.0$ ps^{-1}. The electron-phonon matrix element controls the influence of the optical phonon on the band dynamics and plays an important role in our model. To study its influence, we present calculations using the values of $g_0^{pd} = 8.0$ meV and $g_0^{pd} = 10.0$ meV in the orbital basis for this matrix element. The optical excitation is patterned after the experimental conditions in Ref. [88] and taken to be a Gaussian pulse with 1.6 eV photon energy, temporal width of $\sigma_T = 14$ fs assuming a Rabi energy $\hbar\Omega_0 = 10$ meV. This results in an excitation of electrons in the conduction band around 200 meV above the unexcited Fermi surface.

After analyzing the consequences of the k-dependent basis transformation we will introduce as a further simplification an averaged value of the electron-phonon matrix element and neglect the influence of the basis transformation. In this case we treat the phonon matrix element as a parameter with $\tilde{g}_0^{cc} = 8.0$ meV.

1. Band and carrier response after optical excitation

Figure 3 shows essential characteristics of the dynamical results via snapshots of the band dynamics and conduction-electron dynamics for the setup with $g_0^{pd} = 10.0$ meV. For this parameter choice, the effects of band renormalization and carrier multiplication are clearly visible. Before the optical excitation the valence band is full and the conduction band nearly empty, as sketched in Fig. 2(a). The band gap of the Mexican-hat-shaped bands is 100 meV at the crease of the Mexican hat $k_0 \simeq 0.35$ nm^{-1}. At around 0 fs the ultrafast optical pulse excites carriers from the lower-lying v' band into the conduction band c at around 200 meV above the unexcited Fermi energy, cf. Fig. 1. Between −25 fs and 25 fs mainly optical excitation occurs but also carrier scattering and the onset of impact ionization. The process of impact ionization is sketched in Fig. 2(b). The combination of these effects and the Mexican-hat band structure lead to a small second peak at the band bottom k_0. Due to the comparatively large band gap of 100 meV, the impact ionization initially is not very efficient. However, after 25 fs, i.e., after the optical excitation is over, the hot carriers in the conduction band lead to a gap closing due to the coherent phonon dynamics and a more efficient screening. The results of Fig. 3 demonstrate that, especially at early times, impact ionization processes, cf. Fig. 2(b) dominate over Auger scattering, cf. Fig. 2(c). In particular, the gap closing leads to a more efficient impact ionization, as will be discussed in detail in connection with Fig. 5. Figure 2 together with Fig. 5 support the following scenario, which is sketched by the sequence of Figs. 2(a)–2(d): Hot carriers relax from a high-energy peak induced by the optical excitation via impact ionization toward a peak at lower energies closer to the band bottom. The impact ionization leads to carrier multiplication in the conduction band, which results in a further gap closing, which is also sketched in Figs. 2(a)–2(d). The smaller gap makes impact ionization even more efficient, which speeds up the relaxation of hot carriers. This is visible in the distances between the snapshots in Fig. 3 but more clearly in Fig. 5 below. Thus there is a mutual amplification between gap closing and impact ionization. The latter occurs predominantly at the band bottom, i.e., at k_0 of the Mexican hat, and thus scatters electrons into the lower energy peak at the band bottom of the conduction band in Fig. 3 until no more phase space for electron-electron scattering is available and a quasiequilibrium distribution is reached, see Fig. 2(d).

We next investigate details of the carrier and band-gap dynamics for the same parameters as in Fig. 3, which are marked by solid black lines in Figs. 4 and 5. We defer a discussion of the different parameters (dashed and red curves in Figs. 4 and 5) to the next subsection. The solid black lines in Fig. 4 shows the carrier distribution of the conduction and valence band 250 fs after the optical excitation. As the optical excitation is into the conduction band, the increase of the hole density around the top of the valence band k_0 in the first 250 fs after the optical excitation indicates the effect of impact ionization as all the carrier dynamics is exclusively due to Coulomb scattering. In Fig. 5 the solid black lines depict the time dependence of the conduction-band carrier density and the band gap. The fast increase of the carrier density due to the ultrafast optical excitation occurs around the center of the pulse at 0 fs. This induces a gap closing via coherent phonons that is clearly visible for times later than 50 fs. Finally, and importantly, there is a delayed increase of the carrier density that is exclusively due to impact ionization from carriers originating from the valence band. This impact ionization therefore effectively acts as carrier excitation mechanism which drives the distributions in the conduction and valence bands further away from equilibrium.

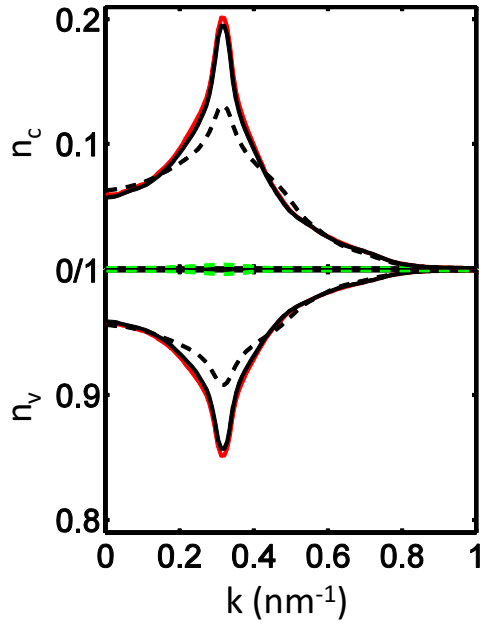

FIG. 4. Carrier distribution in the conduction and valence band before and long after the pulse. $t = -25$ fs (green dashed line) and $t = 250$ fs for the setup with $g_0^{pd} = 10.0$ meV (solid black line), $g_0^{pd} = 8.0$ meV (dashed black line), and $\tilde{g}_0^{cc} = 8.0$ meV (solid red line). As electrons are optically excited into the conduction band, the valence band dynamics are exclusively due to interband scattering, i.e., carrier multiplication. The setups with $g_0^{pd} = 10.0$ meV and $\tilde{g}_0^{cc} = 8.0$ meV exhibit similar carrier distributions after 250 fs.

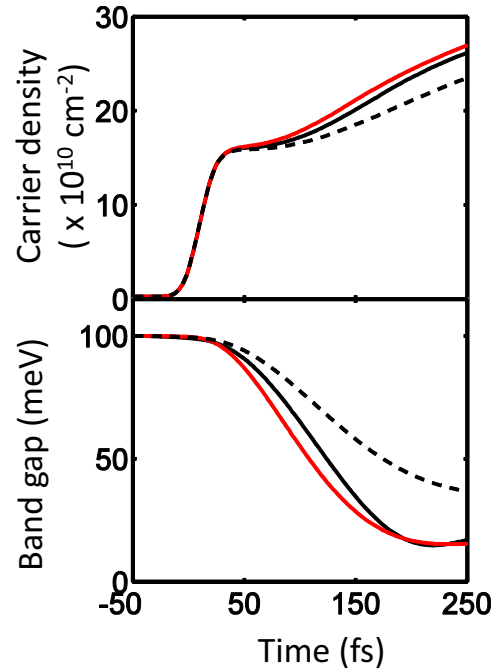

FIG. 5. Gap closing (bottom) and carrier density in the conduction band (top) vs time. After the optical excitation an induced gap closing and a delayed carrier multiplication correlated to the gap closing is visible for the setup with $g_0^{pd} = 8.0$ meV (dashed black line), $g_0^{pd} = 10.0$ meV (solid black line), and $\tilde{g}_0^{cc} = 8.0$ meV (solid red line). The setup with $g_0^{pd} = 10.0$ meV and $\tilde{g}_0^{cc} = 8.0$ meV have a similar time evolution of the carrier density and the gap closing. Between 100 fs and 200 fs (short times after optical excitation) only small derivations are visible, which vanish after 200 fs.

The coupling of the nonequilibrium carriers to the coherent phonon increases the band-gap shrinkage further.

2. Influence of electron-phonon matrix elements on response

In Figs. 4 and 5 we study the influence of the electron-phonon coupling and also the consequence of using an averaged value of the phonon matrix element $\tilde{g}_0$. We first replace the electron-phonon matrix elements $g_0^{pd} = 10$ meV used so far by an averaged matrix element $\tilde{g}_0^{cc} = 8.0$ meV. With this replacement, we obtain similar final carrier distributions after 250 fs as shown in Fig. 4, similar carrier densities and band-gap dynamics as shown in Fig. 5 and thus also a similar carrier multiplication of slightly above 70% at 250 fs. To show the sensitivity of the results on the electron-phonon coupling matrix element, we also show a calculation with $g_0^{pd} = 8.0$ meV. This leads to a sizable difference in the final carrier distributions, reduces the band-gap shrinkage and also the carrier multiplication to about 50% for the setup with $g_0^{pd} = 8.0$ meV. Therefore, for a simulation of real materials and their electron-phonon matrix elements it is important to take into account the basis transformation. However, in the spirit of our model, we will use averaged electron-phonon matrix elements, which are capable of reproducing the dynamical calculations, albeit for a slightly different value of the electron-phonon matrix elements. This is sufficient for the more qualitative analysis of the present paper.

In Fig. 6 we analyze the influence of different values of the averaged electron-phonon coupling matrix element $\tilde{g}_0$ by comparing $\tilde{g}_0^{cc} = 8.0$ meV, 4.0 meV, and 6.0 meV. Because the quenching of the insulator phase is due to the coherent phonon dynamics, the gap closing depends on the strength of the electron-phonon matrix. Due to efficiency of the coupling between carrier and band dynamics, the mutual amplification between impact ionization and gap closing leads to a gap minimum of 15 meV for the setup with $\tilde{g}_0^{cc} = 8.0$ meV and 58 meV for the setup with $\tilde{g}_0^{cc} = 6.0$ meV and 81 meV for the setup with $\tilde{g}_0^{cc} = 4.0$ meV. Besides the gap closing also the carrier multiplication is visible in Fig. 6 via the time evolution of the carrier density in the conduction band. After 300 fs a carrier multiplication of 74% ($\tilde{g}_0^{cc} = 8.0$ meV), 42% ($\tilde{g}_0^{cc} = 6.0$ meV), and 26% ($\tilde{g}_0^{cc} = 4.0$ meV) is reached.

C. Comparison to experimental results and influence of different excitation scenarios

An important objective of this paper is to provide results that can be compared with recent experimental photoemission data. In particular, the energy distribution curves of photoemitted electrons cannot unambiguously be interpreted without some theoretical model [88]. As we cannot compute the cross sections that would be needed for a quantitative comparison with the energy distribution curves, we present a qualitative comparison using a broadening of the conduction and valence distribution by the typical experimental energy resolution of 150 meV (FWHM). The broadened distributions

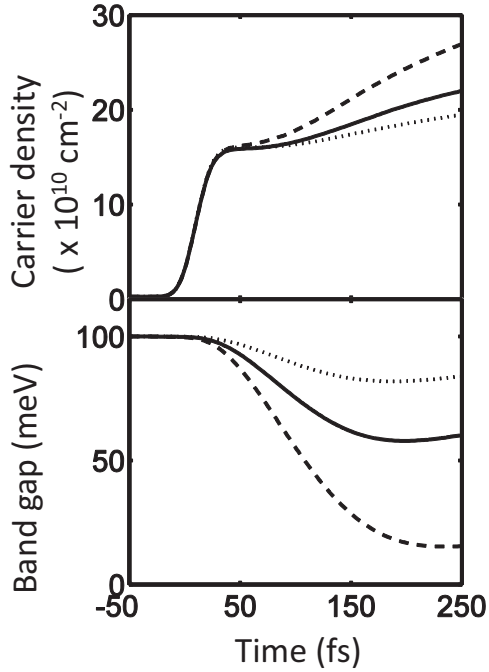

FIG. 6. Gap closing (bottom) and carrier density in the conduction band (top) vs time for setups with averaged phonon matrix elements of 4.0 meV (dotted), 6.0 meV (solid), and 8.0 meV (dashed).

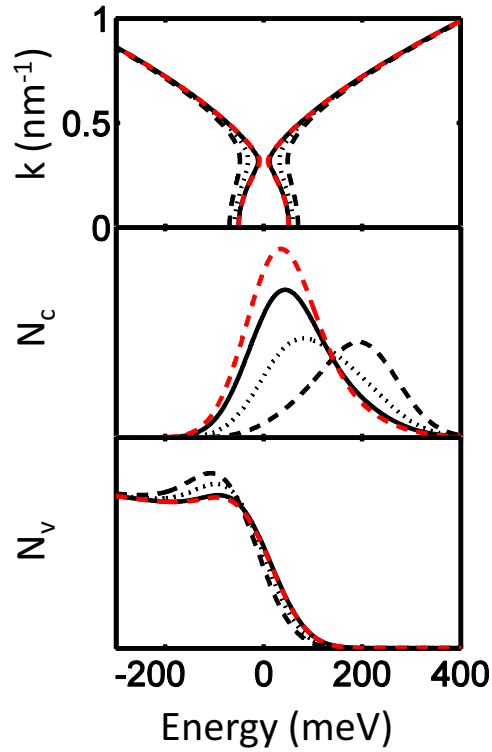

FIG. 7. Time-dependent band dispersion (top), broadened carrier distribution function in the conduction band (middle), and valence band (bottom) at 25 fs (dashed black), 100 fs (dotted black), 175 fs (solid black), and 250 fs (dashed red) after an ultrashort optical excitation at 0 fs. After 200 fs a quasiequilibrium is almost reached in both bands. The dynamics of the distribution function in the valence band is mainly due to the gap closing and reshaping of the bands as the effect of impact ionization is hardly visible due to the broadening. Note that for a better comparison between the N_c and N_v curves, N_c has been multiplied by a factor of 16.

are defined by

$$N_b(E) = \sum_{\mathbf{k}} n^b_{\mathbf{k}}\, g_{\Delta E}\big(\epsilon^b_{\mathbf{k}} - E\big), \tag{18}$$

where $g_{\Delta E}(\epsilon^b_{\mathbf{k}} - E)$ is a Gaussian of width ΔE. The important point for the comparison with experiment are the energy-dependent features, not the numerical value of the N_bs.

In the following, we first illustrate the spectral and kinetic response with the help of the broadened distributions using our two-band model and the electron-phonon matrix element $g^{pd}_0 = 10.0$ meV in the orbital basis including the basis transformation of the electron-phonon matrix elements. We first show results for our model using the band gap of $TiSe_2$ in the charge-density wave phase which are intended to be compared to electron distribution curves for small band-gap materials. Afterward we analyze the dependence of the response on the optical excitation by a parameter study for different Rabi frequencies and excitation energies.

The broadened distributions for conduction and valence bands, together with the band dispersions are shown in Fig. 7 for different times. We focus on the distribution of conduction electrons first. In the first 25 fs, the ultrafast optical excitation creates a peak in this distribution function at 200 meV above the Fermi energy. After 100 fs the hot-carrier relaxation due to impact ionization induced by the gap closing is clearly visible in the broadened distribution function. However, in a Mexican-hat-shaped band structure the interpretation of the broadened electron distribution is not straightforward because a time-dependent increase in the conduction band is a combination of band-dispersion effects and the on-going carrier multiplication. As we have seen in Figs. 4 and 5 the effects of carrier multiplication dominate the increase of the carrier signal at later times. The mutual amplification between impact ionization and gap closing, which has already been discussed, continues as shown by the snapshots for the band and distribution functions in Fig. 7 until there is no more phase space for electron-electron scattering available and a quasiequilibrium distribution is reached after 250 fs. Starting from a value of the band gap that is realistic for a small band-gap material like $1T$-$TiSe_2$ we thus obtain in our model calculation a signal of ultrafast carrier dynamics that is in agreement with experimental results, such as those reported in Ref. [88]. Our calculated "signal" can be explained in terms of a mutual amplification between gap closing, which goes along with the quenching of the insulator phase, and impact ionization. In the present paper, the band-gap dynamics are due to coherent phonons and are therefore applicable to a Peierls-like insulator. It is to be expected that a similar connection between gap closing and impact ionization occurs also for an excitonic-insulator phase-change mechanism. It may be even more pronounced in the excitonic-insulator case, because there the characteristic response times are faster than the response time of a Peierls insulator, cf. Ref. [14], which indicates that the important electron-electron coupling matrix elements in that case are larger. However, because of the slower gap

response in the Peierls (electron-phonon coupling) case, the connection between gap closing and carrier multiplication can be more easily disentangled in the model used here.

Turning to the broadened valence band distributions, shown in Fig. 7(bottom), the holes at the top of the Mexican-hat-shaped valence band created by impact ionization are hardly visible. This is because the broadening of the distribution function almost completely removes the dip in the microscopic valence band distributions n_v shown in Fig. 4. This is in agreement with our earlier study using a parabolic valence band and experimental results in Ref. [88]. The dynamics of the Mexican hat introduces new features, such as the bump of the broadened valence band distribution around the top of the filled valence band, which is due to the changing band dispersion. The shift of the broadened distribution function is due to the band shift of the valence band as shown in Fig. 7(top). These results give a simple microscopic picture of electronic dynamics underlying the electron distribution curves observed, e.g., in Ref. [88] for $TiSe_2$. We plot and discuss the band and carrier dynamics in this paper up to about 250 fs, which is the onset of the phase transition. At longer times the system can go further into a different phase where the back-folded valence band disappears or the system can return to the insulator phase by cooling processes due to carrier-phonon scattering. Both effects are not included in the present study and are left for future investigations.

After analyzing the characteristic response of the system, we study its dependence on the optical excitation by varying the Rabi frequency and photon energy of the ultrafast optical excitation. The quantitative differences between a calculation with and without the electron-phonon basis transformation are insignificant for this analysis, and for the sake of simplicity, we use an averaged electron-phonon matrix element $\tilde{g}_0^{cc} = 6.0$ meV. We take this as a reference value in the following parameter study as it is an intermediate value of the coupling so that a reduction and an increase still show an interesting gap closing dynamics. The value of $g_0^{pd} = 10.0$ was chosen in Fig. 7 because it exhibits a relatively fast dynamics (of the gap closing and the carrier dynamics) for which structures in the distribution function are most easily visible.

In Fig. 8 we compare different excitation photon energies, which lead to different energies at which the electrons are created in the conduction band. We call this the excitation energy E_X and measure it from the unexcited Fermi energy E_F, as sketched in Fig. 3. We analyze the cases of $E_X =$ 150 meV, 200 meV (which has been used so far and constitutes our reference setup in the following), and 250 meV. For the setup with $E_X - E_F = 250$ meV, carriers are excited around 200 meV above the conduction-band bottom; the distance to the band bottom is reduced to 100 meV for the setup with $E_X - E_F = 150$ meV. As shown in Fig. 8(top) the carrier density created during the optical pulse in the conduction band is only slightly different for the three setups, but its subsequent time evolution is different. However, the corresponding band gap changes for the different excitation energies in Fig. 8(bottom) deviate only by around 20 meV, i.e., 10 meV for each band, which is much smaller than the difference of the excitation energies. The most important contribution to the difference in carrier densities for the three excitation energies must therefore be due to different carrier

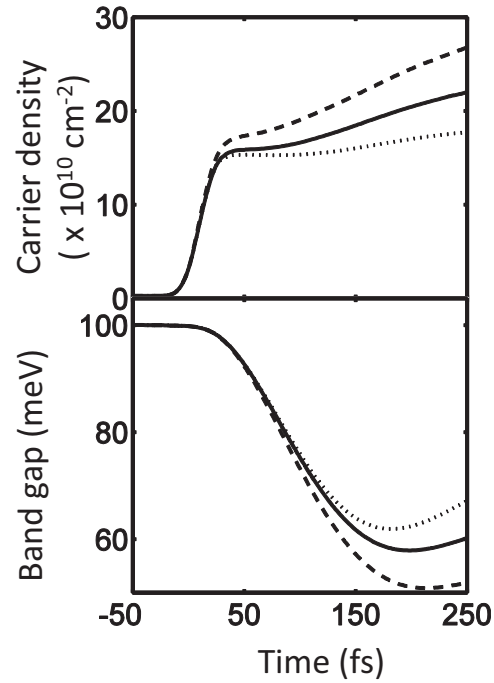

FIG. 8. Gap closing (bottom) and carrier density in the conduction band (top) vs time for different excitation energies of 150 (dotted), 200 (solid), and 250 (dashed) meV above the Fermi energy.

multiplication effects, and the impact ionization is most efficient for the setup with $E_X - E_F = 250$ meV. Figure 8 further shows that the efficiency of the mutual amplification between impact ionization and gap closing increases nonlinearly. After 250 fs the values for the the carrier multiplication are 73%, 42%, and 14%, respectively, for the excitation energies of $E_X - E_F = 250$, 200, and 150 meV. The corresponding band gaps are 52, 60, and 67 meV. This nonlinearity is mainly due to repeated interband scattering processes that become possible for electrons excited at higher energies. During their scattering dynamics toward the band bottom these electrons can contribute to the carrier multiplication process twice or more times.

In Fig. 9 we investigate the dependence of the dynamics on the excitation strength. We compare three amplitudes of the Rabi energy $\hbar\Omega_0$: 6.6, 10.0 (our reference setup and the value used so far), and 15.0 meV. In contrast to Fig. 8, the carrier density created in the conduction band by the optical excitation is different for the three cases. The carrier density is the driving force of the coherent-phonon amplitude, which induces an atomic displacement responsible for the band-gap dynamics, so that we obtain a higher initial band-gap reduction for larger values of $\hbar\Omega_0$ and this band gap remains smaller due to the mutual amplification between gap closing and impact ionization. The gap closing evidently saturates in Fig. 9(bottom). The effect of impact ionization can be assessed from the carrier multiplication in Fig. 9(top), which is 33%, 42%, and 43%, respectively, for Rabi energies $\hbar\Omega_0 =$ 6.6, 10.0, and 15 meV. This carrier multiplication shows only a comparatively small increase between the two smaller Rabi energies, whereas we have a pronounced difference in the gap closing. The difference between the dynamical scenarios

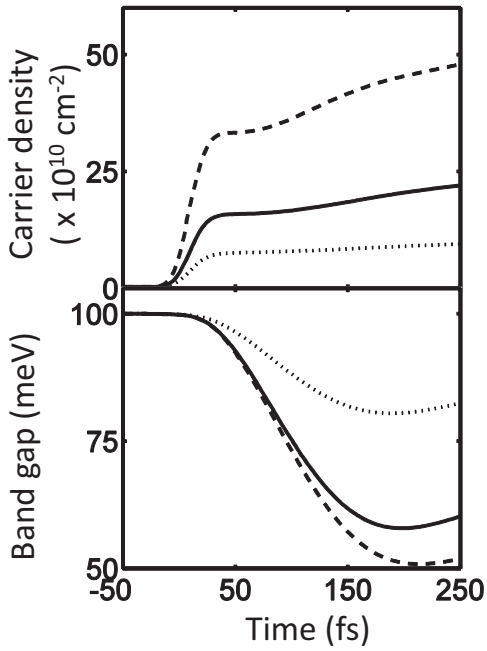

FIG. 9. Gap closing (bottom) and carrier density in the conduction band (top) vs time for different Rabi energies of 6.6 (dotted), 10.0 (solid), and 15.0 (dashed) meV.

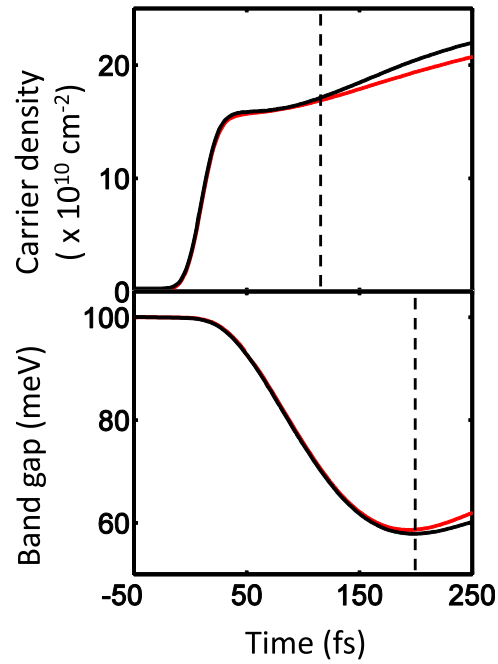

FIG. 10. Gap closing (bottom) and carrier density in the conduction band (top) vs time for a parabolic (red) and a Mexican-hat-shaped (black) band with phonon matrix element $\tilde{g}_0^{cc} = 6.0$ meV.

shown in Fig. 9 is therefore mainly due to the different gap closing related to the initial photoexcited carrier density and the saturation of the gap closing is mainly responsible for the saturation of the carrier multiplication. Parenthetically, we remark that a saturation of the gap quenching of the charge-density wave state has been observed in the charge-density wave material RTe_3 where only an incomplete suppression of the charge-density wave occurs; here we find an indication of a saturation for comparatively small electron-phonon coupling [93].

D. Influence of different band shapes

As mentioned, we are interested in elucidating the influence of the band structure on measurable quantities, in particular energy distribution curves produced by photoemission experiments. In order to understand the calculated broadened distribution functions that can be compared with experiment, we here first discuss the influence of the band shape on the carrier dynamics without added broadening and use for the comparison a parabolic band and the Mexican-hat-shaped band that we have based our calculations on so far. For a meaningful comparison, we define the parabolic band setup using all band parameters of the Mexican-hat-like band setup, except a change of the on-site energies ϵ_0^p and ϵ_0^d from 1.95 to 2.0 eV. In this way, the parabolic and the Mexican-hat-shaped bands have the same band gap, but in the parabolic case it occurs at $k = 0$ and in the Mexican-hat band case at k_0. The band structures are plotted in Figs. 12(top) and 13(top) as dotted lines.

In Figs. 10 and 11 the gap closing and carrier density in the conduction band vs time is shown for the parabolic and Mexican-hat-shaped band structures with $\tilde{g}_0^{cc} = 6.0$ meV and $\tilde{g}_0^{cc} = 8.0$ meV, respectively. Due to the different band shape, the "tuning" of the band dispersion and the optical excitation is slightly different. We have already seen in Fig. 8 that such a small difference in excitation energy will also lead to a slightly different optically excited carrier density for the two band structures. However, the further time evolution of the carrier density is mainly determined by the different band dispersions. The origin of the steeper band dispersion for

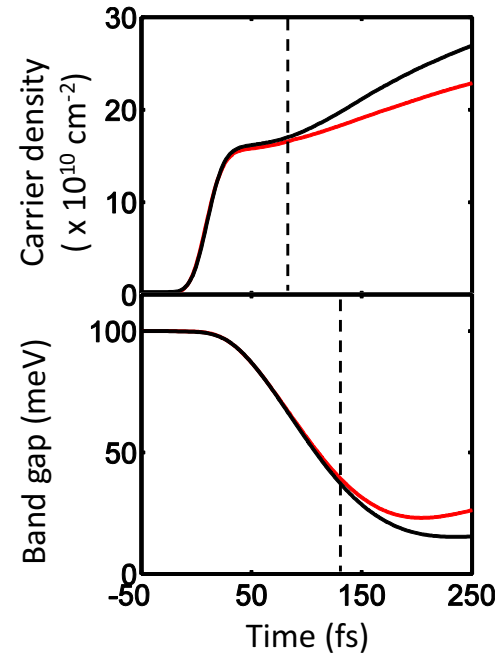

FIG. 11. Gap closing (bottom) and carrier density in the conduction band (top) vs time for a parabolic (red) and a Mexican-hat-shaped (black) band with phonon matrix element $\tilde{g}_0^{cc} = 8.0$ meV.

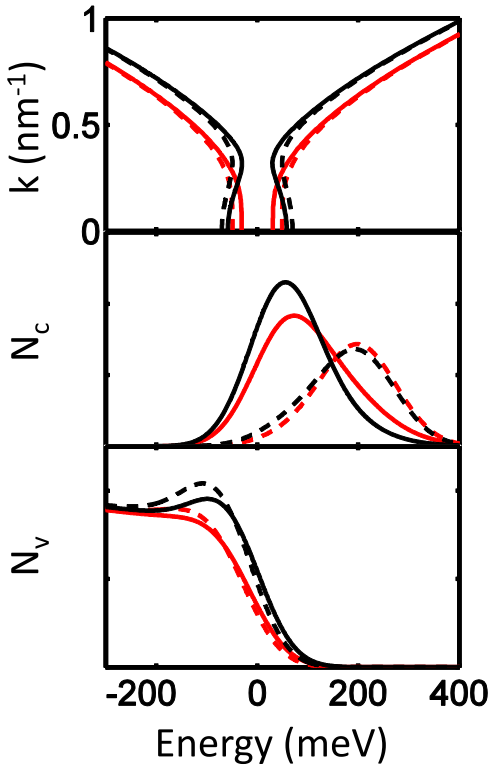

FIG. 12. Band dynamics (top) and broadened carrier distribution function in the conduction band (middle) and valence band (bottom) at 25 fs (dashed) and 250 fs (solid) after an ultrashort optical excitation at 0 fs for a parabolic (red) and a Mexican-hat-shaped (black) band with phonon matrix element $\tilde{g}_0^{cc} = 6.0$ meV.

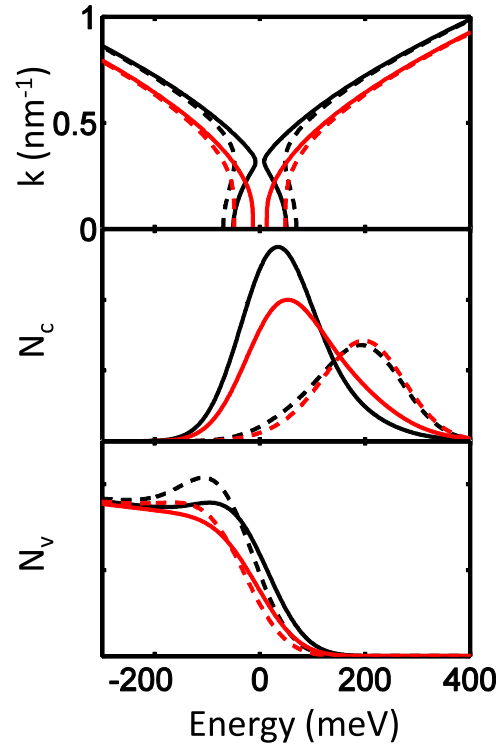

FIG. 13. Band dynamics (top) and broadened carrier distribution function in the conduction band (middle) and valence band (bottom) at 25 fs (dashed) and 250 fs (solid) after an ultrashort optical excitation at 0 fs for a parabolic (red) and a Mexican-hat-shaped (black) band with phonon matrix element $\tilde{g}_0^{cc} = 8.0$ meV.

the Mexican-hat-shaped band is the characteristic band-gap minimum at a $k_0 \neq 0$ (i.e., not at the high-symmetry point) and a local band-gap maximum at $k = 0$ (the high symmetry point) in contrast to the parabolic case, where the global band gap minimum is at $k = 0$. The efficiency of the impact ionization depends on the size of the band gap and the k-dependent Bloch wave functions, which include band mixing effects, as well as the available phase space for the scattering process. The band mixing is connected to the position of the band-gap minimum and, thus, different between the parabolic and Mexican-hat setups.

These qualitative differences between the band structures should lead to different carrier dynamics, and we compare these dynamics in Figs. 10–13. In a parabolic band, the hot carriers relax directly into the high-symmetry $k = 0$ point, while in the case of the Mexican-hat-shaped band, hot carriers relax more into the band minimum k_0 and reach the local maximum at the high-symmetry $k = 0$ point only with a delay. Therefore, band-gap minima on different k positions combined with a different k dependence of the available phase space results in different efficiency for impact ionization for equal band-gap minima. We first focus on Figs. 10 and 11 where we compare the gap closing and conduction-band carrier density between Mexican-hat and parabolic bands for different electron-phonon couplings. A higher impact ionization efficiency for the Mexican-hat-shaped band induces a difference in the carrier density between the two band structures, as can be seen from splitting of the curves above 100 fs in Figs. 10 and 11, respectively. The mutual amplification between impact ionization and band-gap closing amplifies the difference in the temporal evolution of the band gap (see splitting of the curves at a slightly later time around 150 fs) and of the impact ionization efficiency. Therefore, the difference between the two band structures increases for band gap and conduction-band carrier density with time. In Fig. 10 this results in a band gap of 60 and 62 meV and a carrier multiplication of 42% and 35% (factor: 1.2) for the Mexican-hat structures compared to the respective calculation with the parabolic bands. In Fig. 11 for the larger electron-phonon coupling $\tilde{g}_0^{cc} = 8.0$ meV we have band gaps of 15 and 26 meV after 250 fs and carrier multiplications of 74% and 50% (factor: 1.5) for the Mexican-hat and parabolic bands, respectively. Depending on the electron-phonon matrix element the influence of the band shape can therefore be substantial.

In Figs. 12 and 13 we compare the time evolution of the band structure and broadened carrier distributions for the Mexican-hat and parabolic bands. As the broadened distributions average over all k states in a given energy range set by ΔE in Eq. (18) they are influenced both by the carrier redistribution dynamics (i.e., carrier multiplication) and by the band structure, especially *if* the band structure changes. In our earlier paper [88], we presented a simple parabolic model without band mixing and without a dynamically changing band structure. With the present calculation for parabolic and Mexican-hat-shaped bands and a consistent inclusion of band

mixing effects, we can investigate the contribution of the dynamical band structure to the electron distribution curves.

Figures 12 and 13 are for different electron-phonon couplings and are obtained from the same dynamical calculations as Figs. 10 and 11, respectively. For a broadening that corresponds to state-of-the-art photoemission experiments, the broadened carrier distributions created by the optical excitation around 25 fs are similar for the Mexican hat and parabolic bands, but a difference of the weighted carrier distribution in the conduction band can be seen after 250 fs. In the parabolic-band case, there are only rigid band shifts and negligible changes in band curvature so that the change in the broadened distribution reflects essentially only the redistribution by scattering processes and the increase in the number of carriers due to carrier multiplication. In the Mexican-hat band structure, there are pronounced changes in the band curvature that also influence the broadened distribution functions. While there are quantitative differences to the parabolic case, we observe a similar behavior of the broadened distribution function that is in qualitative agreement with the carrier multiplication factors determined from Figs. 10 and 11. We conclude that the behavior of computed broadened distribution functions, which are the quantity we compare to experimental electron-distribution curves and which are similar to experimental results on $TiSe_2$, are an unambiguous indicator of carrier multiplication. The energy-dependent signatures found in Figs. 12 and 13 are only influenced to a small extent by changes in the spectral properties of the carriers, even though the dynamical changes in the curvature of the Mexican-hat band-structure model likely overestimate those occurring in a real small band-gap material.

In the valence band, a characteristic bump below the Fermi energy appears only in the broadened distribution function in the Mexican-hat-shaped band. The erosion of this bump, which is not visible in the parabolic band, indicates the effect of carrier multiplication. In $TiSe_2$ the Se $4p$ band, as opposed to the Ti $3d$, does not show a Mexican-hat-like structure and therefore it is difficult to observe characteristics of impact ionization in the valence band with the energy broadening introduced by current experimental photoemission setups. Because the temporal evolution of the valence band signal is more influenced by the band and less influenced by the carrier dynamics, the difference between different band shapes, in particular in Fig. 12, is more pronounced than the differences between the two snapshots at different times.

V. CONCLUSION

Motivated by recent experimental time-resolved photoemission studies of the carrier and band dynamics in 1T-$TiSe_2$, we investigated carrier multiplication dynamics due to impact ionization after ultrafast optical excitation in a model band structure of a quasi-two-dimensional material with small band gaps. We analyzed the coupling to coherent phonons, which mimics the *onset* of the quenching of the insulator phase, as a concrete mechanism for the photo-induced band-gap narrowing close to the Fermi surface. An important goal of our study was to explore the consequences of the combined carrier and band-structure dynamics on experimentally accessible quantities, in particular electron distribution curves.

We used a dynamical approach that includes time-dependent band energies and wave functions, which make the Coulomb-matrix elements and the static screening effectively time dependent. Using this model, we were able to quantify the contribution of impact ionization in the ultrafast response of small band-gap 2D materials and discussed the importance of the *interplay* between carrier and band dynamics. We discussed the signatures of impact ionization and gap closing in photoemission electron-distribution curves. We also investigated the influence dynamical changes in the band curvature, as these changes will also influence energy distribution curves and cannot, at present experimental resolutions, be distinguished from carrier multiplication effects. To this end, we compared a parabolic band structure with that of a Mexican hat and found that the characteristic change in energy distribution curves in, e.g., $TiSe_2$ [88], are indeed mainly due to carrier multiplication effects, and only to a small extent due to changes in the spectral function of the electrons. Our computed energy-dependent distribution curves compare well with experiments on $TiSe_2$. Although we consider a specific coupling mechanism to a coherent phonon and have not yet included excitonic effects, we believe that our results capture a general trend in small band-gap 2D materials as far as carrier multiplication vs band gap dynamics go.

APPENDIX A: TIGHT-BINDING MODEL

For our tight-binding model we assume a quasi-two-dimensional material like TMDCs with two kind of atoms A_d and A_p. In the case of a TMDC, atom sort A_d would be the transition metal atom (e.g., Ti) with d-type or f-type valence orbital and atom sort A_p would be the chalcogen atoms (e.g., Se) with p-type valence orbitals. The unit cell would consist of one A_d and two A_p atoms. For example, the lattice vectors $L_1 = (l_1, -l_2, 0)$, $L_2 = (l_1, l_2, 0)$, and $L_2 = (0, 0, l_3)$ would span a unit cell with the atom basis $B_d = (0, 0, 0)$ for A_d, $B_{p,1} = (b_1, b_2, b_3)$ for the first A_p, and $B_{p,2} = (b_1, b_2, -b_3)$ for the second A_p. The nearest-neighboring A_d or A_p atoms in the same plane would have a hexagonal or tetragonal symmetry. To model an accurate band structure for a TMDC around the Fermi surface the three t_{2g} (i.e., d_{xy}, d_{zx}, d_{xy}) and eventually the energetically higher two e_g (i.e., $d_{3z^2-r^2}$, $d_{x^2-y^2}$) orbitals of the atom of sort A_d and the six p-orbitals of the two atoms of sort A_p might be considered [76].

Weak interactions between neighboring orbitals are usually neglected and the remaining interactions are expressed in terms of Slater-Koster integrals [94]. The bond integrals between two orbitals are distinguished among σ, π, or eventually δ bondings. For example, as described in Refs. [74,76] for $TiSe_2$, only the three hopping pathways dd_σ, pp_σ, and pd_π contribute significantly to the behavior of charges close to the Fermi energy. The resulting band structure around the high-symmetry points under investigation of the small band-gap TMDCs is often highly unisotropic like in $TiSe_2$ as reported, e.g., in Ref. [60]. For this material, the nonisotropic band dispersion of the Ti $3d$ band is nonparabolic, i.e., an ellipsoid, and has a Mexican-hat-shaped geometry in the CDW insulator phase.

Regarding the investigated band dynamics of such a material in the insulator phase, we avoid a material realistic

description, where the insulator phase is determined from the normal phase, to investigate the role of different kinds of interactions in the phase transition. Instead, we model the TB Hamiltonian already in the insulator phase and describe the band dynamics via an effective atomic displacement as disturbance of the insulator phase. To model the small band gap around the Fermi surface, we use a simple two-band tight-binding model capable to describe the characteristics of the carrier and band dynamics of such a material after an ultrashort optical excitation. Thus, we obtain an isotropic band shape around a high-symmetry point. The validity of this assumption is additionally motivated at the end of this section.

To transform a more material-realistic TB model into a simpler model with high symmetry capable of describing the characteristics of the carrier and band dynamics close to the important high-symmetry point, a lot of more- or less-sophisticated transformation can be done. A simple way of doing it is to disregard the t_{2g} and to consider only one d orbital, e.g., d_{xy}, of A_d and one p orbital, e.g., p_y, of A_p and give only $V_{pp\sigma}$, $V_{dp\sigma}$, and $V_{dd\sigma}$ finite values. In the spirit of such a transformation, we use the following effective tight-binding Hamiltonian to describe the investigated small band-gap insulator phase:

$$\begin{aligned} H_{\mathrm{TB}} = {} & \epsilon_0^p c_{\mathbf{k}}^{ps\dagger} c_{\mathbf{k}}^{ps} + \epsilon_0^c \left(c_{\mathbf{k}}^{ds}\right)^\dagger c_{\mathbf{k}}^{ds} \\ & + 2V_{pp}[\cos(k_x e_x) + \cos(k_y e_y)] \left(c_{\mathbf{k}}^{ps}\right)^\dagger c_{\mathbf{k}}^{ps} \\ & + V_{pd} e^{-i\mathbf{k}\cdot\mathbf{d}_{pd}} \left(c_{\mathbf{k}}^{ps}\right)^\dagger c_{\mathbf{k}}^{ds} + V_{dp} e^{i\mathbf{k}\cdot\mathbf{d}_{pd}} \left(c_{\mathbf{k}}^{ds}\right)^\dagger c_{\mathbf{k}}^{ps} \\ & + 2V_{dd}[\cos(k_x e_x) + \cos(k_y e_y)] \left(c_{\mathbf{k}}^{ds}\right)^\dagger c_{\mathbf{k}}^{ds}, \end{aligned} \tag{A1}$$

where ϵ_0^p, ϵ_0^d are the on-site energies; V_{pp}, $V_{pd} = V_{dp}$, V_{dd} are the tight-binding coupling-elements; and $\mathbf{d}_{pd}$ is the relative distance vector between the two effective atoms within the unit cell. As we do not include spin-orbit coupling, we do not explicitly write out the spin dependence in the following. The outcome is a conduction band mainly originating from a d-type transition metal orbital and a valence band mainly originating from a p-type chalcogen orbital. In the region of the examined high-symmetry point, we obtain an angular symmetric Mexican-hat-shaped band with a small band gap and a high band mixing. However, assuming a fast angular redistribution of carrier via electron-phonon scattering as, e.g., reported in Ref. [89], the fundamental results of this investigation are also transferable to nonparabolic band structures.

APPENDIX B: BASIS TRANSFORMATION OF THE PHONON MATRIX ELEMENTS

The Hermitian Hamiltonians in Eq. (1) and (4) are real and symmetric with real eigenvalues and eigenstates. The eigenstates form the orthogonal matrix U which describes the transformation from the orbital basis to the band basis. Without loss of generality, the orthogonal matrix U can be written in the form

$$R = \begin{bmatrix} \cos(\alpha) & -\sin(\alpha) \\ \sin(\alpha) & \cos(\alpha) \end{bmatrix}. \tag{B1}$$

The basis transformation of the phonon matrix

$$g_{\mathrm{pn}}^{pd} = \begin{pmatrix} 0 & g_{\mathrm{pn}}^0 \\ g_{\mathrm{pn}}^0 & 0 \end{pmatrix} \tag{B2}$$

into cv basis is

$$g_{\mathrm{pn}}^{cv} = U^\dagger g_{\mathrm{pn}}^{pd} U. \tag{B3}$$

Analytically, we obtain with the representation R for the orthogonal matrix U

$$g_{\mathrm{pn}}^{cv} = R^{-1} g_{\mathrm{pn}}^{pd} R = \begin{pmatrix} g_{\mathrm{pn}}^{pd}\big|_d & g_{\mathrm{pn}}^{pd}\big|_{nd} \\ g_{\mathrm{pn}}^{pd}\big|_{nd} & -g_{\mathrm{pn}}^{pd}\big|_d \end{pmatrix}, \tag{B4}$$

where

$$\begin{aligned} g_{\mathrm{pn}}^{pd}\big|_d &= 2\cos(\alpha)\sin(\alpha) g_{\mathrm{pn}}^0 \\ g_{\mathrm{pn}}^{pd}\big|_{nd} &= [\cos^2(\alpha) - \sin^2(\alpha)] g_{\mathrm{pn}}^0. \end{aligned} \tag{B5}$$

Thus, the basis rotation results in a sign change for the diagonal matrix elements of the basis transformed matrix for all values of α.

APPENDIX C: EQUATION OF MOTION IN THE TIME-DEPENDENT EIGENBASIS

We start from the total Hamiltonian

$$H_{\mathrm{tot}} = H_{\mathrm{qp}} + H_{\mathrm{int}}, \tag{C1}$$

consisting of a quasiparticle Hamiltonian H_{qp} and an interaction Hamiltonian H_{int}. If the quasiparticle part is time dependent, as discussed in Sec. II B, where $H_{\mathrm{qp}} = H_{\mathrm{eff}} = H_{\mathrm{CohPh}} + H_{\mathrm{TB}}$, then the eigenvalues and eigenvectors of this Hamiltonian have to be calculated for every time step of the dynamical calculation. Such a time-dependent basis is associated with a basis transformation of the whole equation of motion for every time step as discussed in the following.

We start using the eigenbasis of quasiparticle Hamiltonian $H_{\mathrm{qp}}(t_0)$ at a time t_0. In this basis the equation of motion for the reduced density matrix $\rho_{\mathbf{k}}^{b_1 b_2} = \langle c_{\mathbf{k}}^{b_2\dagger} c_{\mathbf{k}}^{b_1} \rangle$ is

$$\frac{d}{dt}\rho_{\mathbf{k}}^{b_1 b_2} = \left.\frac{d\rho_{\mathbf{k}}^{b_1 b_2}}{dt}\right|_{\mathrm{qp}} + \left.\frac{d\rho_{\mathbf{k}}^{b_1 b_2}}{dt}\right|_{\mathrm{int}}. \tag{C2}$$

The quasiparticle part of the equation of motion can be written as

$$\left.\frac{d\rho_{\mathbf{k}}^{b_1 b_2}}{dt}\right|_{\mathrm{qp}} = h_{\mathbf{k}}^{b_1 b_2}\rho_{\mathbf{k}}^{b_1 b_2} - h_{\mathbf{k}}^{b_2 b_1}\rho_{\mathbf{k}}^{b_2 b_1} \tag{C3}$$

and the interaction part can be written in the general form of

$$\left.\frac{d\rho_{\mathbf{k}}^{b_1 b_2}}{dt}\right|_{\mathrm{int}} = \sum \Gamma[\rho], \tag{C4}$$

i.e., a sum over correlation contributions Γ, which are functionals of the density matrices ρ.

For a time $t_1 > t_0$, the equation of motion $\frac{d}{dt}\tilde{\rho}_{\mathbf{k}}^{b_1 b_2}$ in the new eigenbasis of the system at time t_1 takes the form

$$\begin{aligned} \frac{d}{dt}\tilde{\rho}_{\mathbf{k}}^{b_1 b_2} &= \frac{d}{dt}[U^\dagger \rho_{\mathbf{k}}^{b_1 b_2} U] \\ &= \frac{dU^\dagger}{dt}\rho_{\mathbf{k}}^{b_1 b_2} U + U^\dagger \frac{d\rho_{\mathbf{k}}^{b_1 b_2}}{dt} U + U^\dagger \rho_{\mathbf{k}}^{b_1 b_2}\frac{dU}{dt}, \end{aligned} \tag{C5}$$

where U is a unitary matrix of the basis transformation between the eigenbasis at the time t_0 and the eigenbasis at the

time t_1. This expression relates the dynamics of the reduced density matrix in the two different single particle bases at different times. It contains a correction term that involves the derivative of the transformation matrix U. We have checked that this contribution is important only if the character of the single-particle states changes significantly, which is not the case during the onset of the phase transition considered here. We will deal with situations involving more pronounced basis changes in a separate paper. Neglecting the time derivative of U yields for the quasiparticle part, we obtain

$$\begin{aligned} U^\dagger \frac{d\rho_{\mathbf{k}}^{b_1b_2}}{dt}|_{\mathrm{qp}} U &= U^\dagger h_{\mathbf{k}}^{b_1b_2} U U^\dagger \rho_{\mathbf{k}}^{b_1b_2} U - U^\dagger T_{\mathbf{k}}^{b_2b_1} U U^\dagger \rho_{\mathbf{k}}^{b_2b_1} U \\ &= \tilde{h}_{\mathbf{k}}^{b_1b_2} \tilde{\rho}_{\mathbf{k}}^{b_1b_2} - \tilde{h}_{\mathbf{k}}^{b_2b_1} \tilde{\rho}_{\mathbf{k}}^{b_2b_1} \\ &= \frac{d\tilde{\rho}_{\mathbf{k}}^{b_1b_2}}{dt}|_{\mathrm{qp}}. \end{aligned} \tag{C6}$$

The transformation of the interaction part can be done in an analogous fashion, but the derivation depends on the level of approximation employed for the interaction. We assume here that the interaction part can finally be written in a general form as

$$\left.\frac{d\tilde{\rho}_{\mathbf{k}}^{b_1b_2}}{dt}\right|_{\mathrm{int}} = \sum \tilde{\Gamma}[\tilde{\rho}]. \tag{C7}$$

One advantage of such a basis transformation is that $\tilde{n}_{\mathbf{k}}^{b} = \tilde{\rho}_{\mathbf{k}}^{bb}$ can be interpreted as the occupation of the state $|b\mathbf{k}\rangle$ at time t_1. Therefore, the intuitive physical picture used in common approximation schemes is preserved. However, the basis transformation is associated with a transformation of diagonal density contributions $n_{\mathbf{k}}^{b}$ into off-diagonal coherence contributions in conjunction with correlated correction terms in the equation of motion as shown above.

In the case of a sufficiently strong dephasing of the coherences, the off-diagonal contributions in conjunction with the correction from the correlation contribution can be neglected in the equation of motion. Then, the carrier occupation adapts instantaneously to the new band structure. We assume that the composition of the bands does not change too fast and approximate the result of this adaptation to be $\tilde{n}_{\mathbf{k}}^{b} \approx n_{\mathbf{k}}^{b}$. We thus implement the time-dependent basis in the description of the carrier dynamics using time-dependent band-energies and wave functions including time-dependent Coulomb-matrix elements due to the basis transformation with a time-dependent screening. The band dynamics here lead to an additional redistribution of carriers into the new equilibrium distribution and a different pronunciation of intra- and interband scattering pathways.

For example, the Coulomb scattering terms for the occupation $\tilde{n}_{\mathbf{k}}^{b}$ at time t_1 can be written as

$$\frac{d}{dt}\tilde{n}_{\mathbf{k}}^{b} = \frac{2\pi}{\hbar} \sum_{\mathbf{k}_2\mathbf{k}_3} \sum_{b_2b_3b_4} \tilde{\tilde{W}}[\tilde{N}^{\mathrm{in}} - \tilde{N}^{\mathrm{out}}]\delta(\Delta\tilde{\epsilon}) \tag{C8}$$

with

$$\tilde{\tilde{W}} = \tilde{W}_{\mathbf{k}\mathbf{k}_2\mathbf{k}_3\mathbf{k}_4}^{bb_2b_3b_4} \left(\tilde{W}_{\mathbf{k}\mathbf{k}_2\mathbf{k}_3\mathbf{k}_4}^{bb_2b_3b_4*} - \tilde{W}_{\mathbf{k}\mathbf{k}_2\mathbf{k}_4\mathbf{k}_3}^{bb_2b_4b_3*}\right), \tag{C9}$$

$$\tilde{N}^{\mathrm{in}} = \left(1 - \tilde{n}_{\mathbf{k}}^{b}\right)\tilde{n}_{\mathbf{k}_2}^{b_2}\left(1 - \tilde{n}_{\mathbf{k}_3}^{b_3}\right)\tilde{n}_{\mathbf{k}_4}^{b_4}, \tag{C10}$$

$$\tilde{N}^{\mathrm{out}} = \tilde{n}_{\mathbf{k}}^{b}\left(1 - \tilde{n}_{\mathbf{k}_2}^{b_2}\right)\tilde{n}_{\mathbf{k}_3}^{b_3}\left(1 - \tilde{n}_{\mathbf{k}_4}^{b_4}\right), \tag{C11}$$

$$\Delta\tilde{\epsilon} = \tilde{\epsilon}_{\mathbf{k}}^{b} - \tilde{\epsilon}_{\mathbf{k}_2}^{b_2} + \tilde{\epsilon}_{\mathbf{k}_3}^{b_3} - \tilde{\epsilon}_{\mathbf{k}_4}^{b_4}. \tag{C12}$$

[1] T. Rohwer, S. Hellmann, M. Wiesenmayer, C. Sohrt, A. Stange, B. Slomski, A. Carr, Y. Liu, L. M. Avila, M. Kalläne, S. Mathias, L. Kipp, K. Rossnagel, and M. Bauer, Nature(London) **471**, 490 (2011).

[2] J. A. Sobota, S. L. Yang, D. Leuenberger, A. F. Kemper, J. G. Analytis, I. R. Fisher, P. S. Kirchmann, T. P. Devereaux, and Z. X. Shen, J. Electron Spectrosc. Relat. Phenom. **195**, 249 (2014).

[3] S. Eich, A. Stange, A. V. Carr, J. Urbancic, T. Popmintchev, M. Wiesenmayer, K. Jansen, A. Ruffing, S. Jakobs, T. Rohwer, S. Hellmann, C. Chen, P. Matyba, L. Kipp, K. Rossnagel, M. Bauer, M. M. Murnane, H. C. Kapteyn, S. Mathias, and M. Aeschlimann, J. Electron Spectrosc. Relat. Phenom. **195**, 231 (2014).

[4] C. L. Smallwood, R. A. Kaindl, and A. Lanzara, Europhys. Lett. **115**, 27001 (2016).

[5] I. Gierz, J. Electron Spectrosc. Relat. Phenom. **219**, 53 (2017).

[6] I. Gierz, J. C. Petersen, M. Mitrano, C. Cacho, E. Turcu, E. Springate, A. Stöhr, A. Köhler, U. Starke, and A. Cavalleri, Nat. Mater. **12**, 1119 (2013).

[7] T. Stroucken, J. H. Grönqvist, and S. W. Koch, Phys. Rev. B **87**, 245428 (2013).

[8] M. T. Mihnev, F. Kadi, C. J. Divin, T. Winzer, S. Lee, C.-H. Liu, Z. Zhong, C. Berger, W. A. de Heer, E. Malic, A. Knorr, and T. B. Norris, Nat. Commun. **7**, 11617 (2016).

[9] F. Kadi, T. Winzer, A. Knorr, and E. Malic, Sci. Rep. **5**, 16841 (2015).

[10] G. R. Bhimanapati, Z. Lin, V. Meunier, Y. Jung, J. Cha, S. Das, D. Xiao, Y. Son, M. S. Strano, V. R. Cooper, L. Liang, S. G. Louie, E. Ringe, W. Zhou, S. S. Kim, R. R. Naik, B. G. Sumpter, H. Terrones, F. Xia, Y. Wang, J. Zhu, D. Akinwande, N. Alem, J. A. Schuller, R. E. Schaak, M. Terrones, and J. A. Robinson, ACS Nano **9**, 11509 (2015).

[11] M. Chhowalla, H. S. Shin, G. Eda, L.-J. Li, K. P. Loh, and H. Zhang, Nat. Chem. **5**, 263 (2013).

[12] D. Voiry, A. Mohite, and M. Chhowalla, Chem. Soc. Rev. **44**, 2702 (2015).

[13] A. Steinhoff, M. Florian, M. Rösner, M. Lorke, T. O. Wehling, C. Gies, and F. Jahnke, 2D Materials **3**, 031006 (2016).

[14] S. Hellmann, T. Rohwer, M. Kalläne, K. Hanff, C. Sohrt, A. Stange, A. Carr, M. Murnane, H. Kapteyn, L. Kipp, M. Bauer, and K. Rossnagel, Nat. Commun. **3**, 1069 (2012).

[15] S. Ghatak, A. N. Pal, and A. Ghosh, ACS Nano **5**, 7707 (2011).

[16] T. Cheiwchanchamnangij and W. R. Lambrecht, Phys. Rev. B **85**, 205302 (2012).

[17] A. Chernikov, C. Ruppert, H. M. Hill, A. F. Rigosi, and T. F. Heinz, Nat. Photon. **9**, 466 (2015).

[18] H. Chen, X. Wen, J. Zhang, T. Wu, Y. Gong, X. Zhang, J. Yuan, C. Yi, J. Lou, P. M. Ajayan *et al.*, Nat. Commun. **7**, 12512 (2016).

[19] A. Steinhoff, M. Florian, M. Rösner, G. Schönhoff, T. O. Wehling, and F. Jahnke, Nat. Commun. **8**, 1166 (2017).

[20] B. H. Moon, J. J. Bae, M.-K. Joo, H. Choi, G. H. Han, H. Lim, and Y. H. Lee, Nat. Commun. **9**, 2052 (2018).

[21] G. Grüner, Rev. Mod. Phys. **60**, 1129 (1988).

[22] X. Zhu, Y. Cao, J. Zhang, E. W. Plummer, and J. Guo, Proc. Natl. Acad. Sci. USA **112**, 2367 (2015).

[23] F. Flicker and J. Van Wezel, Nat. Commun. **6**, 7034 (2015).

[24] D.-N. Cho, J. van den Brink, H. Fehske, K. W. Becker, and S. Sykora, Sci. Rep. **6**, 22548 (2016).

[25] M. Leroux, L. Cario, A. Bosak, and P. Rodière, Phys. Rev. B **97**, 195140 (2018).

[26] Y. Nakata, K. Sugawara, S. Ichinokura, Y. Okada, T. Hitosugi, T. Koretsune, K. Ueno, S. Hasegawa, T. Takahashi, and T. Sato, NPJ 2D Mater. Appl. **2**, 12 (2018).

[27] S. Wall, D. Wegkamp, L. Foglia, K. Appavoo, J. Nag, R. Haglund, J. Stähler, and M. Wolf, Nat. Commun. **3**, 721 (2012).

[28] T. Mizokawa, K. Takubo, T. Sudayama, Y. Wakisaka, N. Takubo, K. Miyano, N. Matsumoto, S. Nagata, T. Katayama, M. Nohara *et al.*, J. Supercond. Novel Magn. **22**, 67 (2009).

[29] S. Sykora, A. Huebsch, and K. W. Becker, Europhys. Lett. **85**, 57003 (2009).

[30] S. Kim, K. Kim, and B. I. Min, Sci. Rep. **5**, 15052 (2015).

[31] T. Ritschel, J. Trinckauf, K. Koepernik, B. Büchner, M. v. Zimmermann, H. Berger, Y. I. Joe, P. Abbamonte, and J. Geck, Nat. Phys. **11**, 328 (2015).

[32] M. Gu and J. M. Rondinelli, Sci. Rep. **6**, 25121 (2016).

[33] A. Khitun, G. Liu, and A. A. Balandin, in *IEEE Transactions on Nanotechnology* (IEEE, Piscataway, 2017), Vol. 16, pp. 860–867.

[34] N. M. Gabor, J. C. Song, Q. Ma, N. L. Nair, T. Taychatanapat, K. Watanabe, T. Taniguchi, L. S. Levitov, and P. Jarillo-Herrero, Science **334**, 648 (2011).

[35] T. Winzer, A. Knorr, and E. Malic, Nano Lett. **10**, 4839 (2010).

[36] D. Brida, A. Tomadin, C. Manzoni, Y. J. Kim, A. Lombardo, S. Milana, R. R. Nair, K. Novoselov, A. C. Ferrari, G. Cerullo *et al.*, Nat. Commun. **4**, 1987 (2013).

[37] J. C. Song, M. S. Rudner, C. M. Marcus, and L. S. Levitov, Nano Lett. **11**, 4688 (2011).

[38] J. H. Strait, H. Wang, S. Shivaraman, V. Shields, M. Spencer, and F. Rana, Nano Lett. **11**, 4902 (2011).

[39] F. Koppens, T. Mueller, P. Avouris, A. Ferrari, M. Vitiello, and M. Polini, Nat. Nanotechnol. **9**, 780 (2014).

[40] K.-J. Tielrooij, J. Song, S. A. Jensen, A. Centeno, A. Pesquera, A. Z. Elorza, M. Bonn, L. Levitov, and F. Koppens, Nat. Phys. **9**, 248 (2013).

[41] T. Winzer and E. Malić, Phys. Rev. B **85**, 241404(R) (2012).

[42] J. C. Johannsen, S. Ulstrup, F. Cilento, A. Crepaldi, M. Zacchigna, C. Cacho *et al.*, Phys. Rev. Lett. **111**, 027403 (2013).

[43] N. M. Gabor, Z. Zhong, K. Bosnick, J. Park, and P. L. McEuen, Science **325**, 1367 (2009).

[44] N. M. Gabor, Acc. Chem. Res. **46**, 1348 (2013).

[45] S. Wang, M. Khafizov, X. Tu, M. Zheng, and T. D. Krauss, Nano Lett. **10**, 2381 (2010).

[46] R. Baer and E. Rabani, Nano Lett. **10**, 3277 (2010).

[47] P. Avouris, Z. Chen, and V. Perebeinos, in *Nanoscience and Technology: A Collection of Reviews from Nature Journals* (World Scientific, Singapore, 2010), pp. 174–184.

[48] L. Yang, S. Wang, Q. Zeng, Z. Zhang, T. Pei, Y. Li, and L.-M. Peng, Nat. Photon. **5**, 672 (2011).

[49] C. Manzoni, A. Gambetta, E. Menna, M. Meneghetti, G. Lanzani, and G. Cerullo, Phys. Rev. Lett. **94**, 207401 (2005).

[50] F. Xia, H. Wang, D. Xiao, M. Dubey, and A. Ramasubramaniam, Nat. Photon. **8**, 899 (2014).

[51] S. Lei, F. Wen, L. Ge, S. Najmaei, A. George, Y. Gong, W. Gao, Z. Jin, B. Li, J. Lou *et al.*, Nano Lett. **15**, 3048 (2015).

[52] D. Kufer and G. Konstantatos, ACS Photon. **3**, 2197 (2016).

[53] J.-H. Kim, M. R. Bergren, J. C. Park, S. Adhikari, M. Lorke, T. Fraunheim, D.-H. Choe, B. Kim, H. Choi, T. Gregorkiewicz *et al.*, arXiv:1801.01675.

[54] L. Yuan, T. Wang, T. Zhu, M. Zhou, and L. Huang, J. Phys. Chem. Lett. **8**, 3371 (2017).

[55] S. Ulstrup, A. G. Cabo, J. A. Miwa, J. M. Riley, S. S. Grønborg, J. C. Johannsen, C. Cacho, O. Alexander, R. T. Chapman, E. Springate *et al.*, ACS Nano **10**, 6315 (2016).

[56] K. Rossnagel, J. Phys.: Condens. Matter **23**, 213001 (2011).

[57] M. Porer, U. Leierseder, J.-M. Ménard, H. Dachraoui, L. Mouchliadis, I. E. Perakis, U. Heinzmann, J. Demsar, K. Rossnagel, and R. Huber, Nat. Mater. **13**, 857 (2014).

[58] K.-W. Zhang, C.-L. Yang, B. Lei, P. Lu, X.-B. Li, Z.-Y. Jia, Y.-H. Song, J. Sun, X. Chen, J.-X. Li, and S.-C. Li, Sci. Bull. **63**, 426 (2018).

[59] C. Monney, H. Cercellier, F. Clerc, C. Battaglia, E. F. Schwier, C. Didiot, M. G. Garnier, H. Beck, P. Aebi, H. Berger, L. Forró, and L. Patthey, Phys. Rev. B **79**, 045116 (2009).

[60] C. Monney, E. F. Schwier, M. G. Garnier, N. Mariotti, C. Didiot, H. Beck, P. Aebi, H. Cercellier, J. Marcus, C. Battaglia, H. Berger, and A. N. Titov, Phys. Rev. B **81**, 155104 (2010).

[61] M. Cazzaniga, H. Cercellier, M. Holzmann, C. Monney, P. Aebi, G. Onida, and V. Olevano, Phys. Rev. B **85**, 195111 (2012).

[62] C. Monney, G. Monney, P. Aebi, and H. Beck, Phys. Rev. B **85**, 235150 (2012).

[63] G. Li, W. Z. Hu, D. Qian, D. Hsieh, M. Z. Hasan, E. Morosan, R. J. Cava, and N. L. Wang, Phys. Rev. Lett. **99**, 027404 (2007).

[64] C. Monney, C. Battaglia, H. Cercellier, P. Aebi, and H. Beck, Phys. Rev. Lett. **106**, 106404 (2011).

[65] A. Kogar, M. S. Rak, S. Vig, A. A. Husain, F. Flicker, Y. I. Joe, L. Venema, G. J. MacDougall, T. C. Chiang, E. Fradkin *et al.*, Science **358**, 1314 (2017).

[66] C. Chen, B. Singh, H. Lin, and V. M. Pereira, Phys. Rev. Lett. **121**, 226602 (2018).

[67] D. Pasquier and O. V. Yazyev, Phys. Rev. B **98**, 235106 (2018).

[68] D. Golež, P. Werner, and M. Eckstein, Phys. Rev. B **94**, 035121 (2016).

[69] K. Rossnagel, L. Kipp, and M. Skibowski, Phys. Rev. B **65**, 235101 (2002).

[70] T. E. Karam, J. Hu, and G. A. Blake, ACS Photon. **5**, 1228 (2018).

[71] H. P. Hughes, J. Phys. C **10**, L319 (1977).

[72] M. Hellgren, J. Baima, R. Bianco, M. Calandra, F. Mauri, and L. Wirtz, Phys. Rev. Lett. **119**, 176401 (2017).

[73] T. E. Kidd, T. Miller, M. Y. Chou, and T.-C. Chiang, Phys. Rev. Lett. **88**, 226402 (2002).

[74] J. van Wezel, P. Nahai-Williamson, and S. S. Saxena, Phys. Stat. Solidi B **247**, 592 (2010).
[75] C. Monney, G. Monney, P. Aebi, and H. Beck, New J. Phys. **14**, 075026 (2012).
[76] J. van Wezel, P. Nahai-Williamson, and S. S. Saxena, Phys. Rev. B **81**, 165109 (2010).
[77] V.-N. Phan, K. W. Becker, and H. Fehske, Phys. Rev. B **88**, 205123 (2013).
[78] H. Watanabe, K. Seki, and S. Yunoki, Phys. Rev. B **91**, 205135 (2015).
[79] R. Bianco, M. Calandra, and F. Mauri, Phys. Rev. B **92**, 094107 (2015).
[80] C. Monney, M. Puppin, C. W. Nicholson, M. Hoesch, R. T. Chapman, E. Springate, H. Berger, A. Magrez, C. Cacho, R. Ernstorfer, and M. Wolf, Phys. Rev. B **94**, 165165 (2016).
[81] M. Maschek, S. Rosenkranz, R. Hott, R. Heid, M. Merz, D. A. Zocco, A. H. Said, A. Alatas, G. Karapetrov, S. Zhu *et al.*, Phys. Rev. B **94**, 214507 (2016).
[82] B. Singh, C.-H. Hsu, W.-F. Tsai, V. M. Pereira, and H. Lin, Phys. Rev. B **95**, 245136 (2017).
[83] J. Ishioka, Y. H. Liu, K. Shimatake, T. Kurosawa, K. Ichimura, Y. Toda, M. Oda, and S. Tanda, Phys. Rev. Lett. **105**, 176401 (2010).
[84] J.-P. Castellan, S. Rosenkranz, R. Osborn, Q. Li, K. E. Gray, X. Luo, U. Welp, G. Karapetrov, J. P. C. Ruff, and J. van Wezel, Phys. Rev. Lett. **110**, 196404 (2013).
[85] A. Silva, J. Henke, and J. van Wezel, Phys. Rev. B **97**, 045151 (2018).
[86] B. Hildebrand, T. Jaouen, M.-L. Mottas, G. Monney, C. Barreteau, E. Giannini, D. R. Bowler, and P. Aebi, Phys. Rev. Lett. **120**, 136404 (2018).
[87] F. Weber, S. Rosenkranz, J.-P. Castellan, R. Osborn, G. Karapetrov, R. Hott, R. Heid, K.-P. Bohnen, and A. Alatas, Phys. Rev. Lett. **107**, 266401 (2011).
[88] S. Mathias, S. Eich, J. Urbancic, S. Michael, A. V. Carr, S. Emmerich, A. Stange, T. Popmintchev, T. Rohwer, M. Wiesenmayer, A. Ruffing, S. Jakobs, S. Hellmann, P. Matyba, C. Chen, L. Kipp, M. Bauer, H. C. Kapteyn, H. C. Schneider, K. Rossnagel, M. M. Murnane, and M. Aeschlimann, Nat. Commun. **7**, 12902 (2016).
[89] M. Mittendorff, T. Winzer, E. Malic, A. Knorr, C. Berger, W. A. de Heer, H. Schneider, M. Helm, and S. Winnerl, Nano Lett. **14**, 1504 (2014).
[90] F. Rossi and K. Kuhn, Rev. Mod. Phys. **74**, 895 (2002).
[91] A. Donkov, I. Eremin, J. Knolle, and M. M. Korshunov, J. Supercond. Nov. Magn. **22**, 37 (2009).
[92] B. Chakraborty, A. Bera, D. V. S. Muthu, S. Bhowmick, U. V. Waghmare, and A. K. Sood, Phys. Rev. B **85**, 161403(R) (2012).
[93] L. Rettig, R. Cortés, J.-H. Chu, I. R. Fisher, F. Schmitt, R. G. Moore, Z.-X. Shen, P. S. Kirchmann, M. Wolf, and U. Bovensiepen, Nat. Commun. **7**, 10459 (2016).
[94] J. C. Slater and G. F. Koster, Phys. Rev. **94**, 1498 (1954).